



Research papers



Performance analysis of a battery thermal management system combining thermoelectric, composite phase change material, and liquid cooling under extreme operating conditions

Ding Luo^{a,b,*}, Zihao Wu^a, Yuying Yan^c, Zeyu Sun^d, Lin Yang^{d,e}, Bingyang Cao^{b,*}

^a Collaborative Innovation Center for Microgrid of New Energy, College of Electrical Engineering & New Energy, China Three Gorges University, Yichang 443000, China

^b Key Laboratory for Thermal Science and Power Engineering of Ministry of Education, Department of Engineering Mechanics, Tsinghua University, Beijing 100084, China

^c Faculty of Engineering, University of Nottingham, University Park, Nottingham NG7 2RD, UK

^d School of Agricultural Engineering, Jiangsu University, Zhenjiang, China

^e School of Automotive and Traffic Engineering, Jiangsu University of Technology, Changzhou, China

ARTICLE INFO

Keywords:

Battery thermal management system
Numerical model
Thermoelectric cooler
Composite phase change material
Extreme operating conditions

ABSTRACT

To maintain optimal operating temperatures for lithium-ion batteries under extreme operating conditions, a battery thermal management system (BTMS) integrating the thermoelectric cooler (TEC), liquid cooling, and composite phase change material (CPCM) is developed. Moreover, a transient numerical model has been established, considering thermal, electrical, and fluid multiphysics fields, to precisely evaluate the system's performance. The outcomes indicate a decrease in both the maximum battery temperature and CPCM liquid fraction as the expanded graphite (EG) mass fraction, TEC cooling input current, and coolant flow speed increase. Furthermore, the temperature difference among batteries exhibits a decrease as the EG mass fraction increases, but experiences an elevation with an increase in both current and coolant flow speed. The BTMS features the lowest power consumption and optimal cooling performance at the EG mass fraction of 12 %, the TEC cooling input current of 3 A, and the coolant flow speed of 0.05 m/s. In preheating situations, the battery pack can achieve a temperature of 293.15 K starting from 263.15 K with the assistance of TEC preheating input currents of 4 A and 5 A, taking 5600 s and 2240 s, respectively, to complete the entire preheating procedure. This study will offer new insights into the advancement of the BTMS, allowing for the control of battery temperatures in high-temperature and high-discharge rate conditions, coupled with preheating at low-temperature.

1. Introduction

Against the backdrop of energy development focused on reducing carbon emissions, new energy vehicles, particularly pure electric and plug-in electric vehicles, have made significant progress, and their success can be attributed in part to the widespread use of lithium-ion batteries, renowned for their exceptional energy density and prolonged cycle life [1,2]. However, during the charging and discharging processes of lithium-ion batteries, internal electrochemical reactions occur, posing potential challenges such as thermal runaway [3]. Typically, the operating temperature significantly affects the cycling life and stability of lithium-ion batteries [4]. To ensure optimal performance, it is recommended to maintain the working temperature of the battery pack within the range of 293.15–323.15 K, while keeping the temperature difference

among battery packs below 5 K [5,6]. In situations where batteries undergo rapid charging, discharge, or operate in high-temperature environments, efficient dissipation of the generated heat becomes challenging [7]. Consequently, developing a reliable and efficient battery thermal management system (BTMS) is of paramount importance.

The BTMS can be classified into four types, namely, air cooling, liquid cooling, phase change material (PCM), and heat pipe-based BTMS [8]. Advancements and extensive commercial applications have been made in the BTMS utilizing air cooling and liquid cooling methods [9], whereas the utilization of PCM and heat pipe-based BTMS has gained significant attention recently due to its distinct advantages in heat transfer [10]. In a PCM-based BTMS, the latent heat of PCMs is harnessed to absorb and store the heat released by batteries, thereby regulating the maximum temperature of the battery pack. Nevertheless, the inherent challenges of low thermal conductivity and constrained

* Corresponding authors.

E-mail addresses: Ding.L@outlook.com (D. Luo), caoby@tsinghua.edu.cn (B. Cao).

<https://doi.org/10.1016/j.est.2024.112679>

Received 24 January 2024; Received in revised form 10 June 2024; Accepted 16 June 2024

Available online 21 June 2024

2352-152X/© 2024 Elsevier Ltd. All rights reserved, including those for text and data mining, AI training, and similar technologies.

Nomenclature*Symbols*

c_p	specific heat, $\text{J}\cdot\text{kg}^{-1}\cdot\text{K}^{-1}$
d	pipe diameter, mm
\vec{E}	electric field density vector, $\text{V}\cdot\text{m}^{-2}$
H	enthalpy, $\text{J}\cdot\text{kg}^{-1}$
h	sensible heat enthalpy, $\text{J}\cdot\text{kg}^{-1}$
Δh	phase change enthalpy, $\text{J}\cdot\text{kg}^{-1}$
I	current, A
\vec{J}	current density vector, $\text{A}\cdot\text{m}^{-2}$
p	pressure, Pa
P	power, W
Q_b	heat source of the battery, W
Q_c	heat absorption of the cold side, W
Q_h	heat release of the heat side, W
\dot{S}	source term
T	temperature, K
v	coolant flow speed, $\text{m}\cdot\text{s}^{-1}$
V	volume, mm^3
k	thermal conductivity, $\text{W}\cdot\text{m}^{-1}\cdot\text{K}^{-1}$

Greek symbols

α	Seebeck coefficient, $\mu\text{V}\cdot\text{K}^{-1}$
σ	electrical conductivity, $\text{S}\cdot\text{m}^{-1}$

β	liquid fraction
γ	latent heat, $\text{J}\cdot\text{kg}^{-1}$
ϕ	electrical potential, V
ρ	density, $\text{kg}\cdot\text{m}^{-3}$
μ	dynamic viscosity, Pa·s

Subscripts

al	aluminum
am	ambient
b	battery
co	copper electrode
l	liquid phase
m	material
n	n-type thermoelectric leg
p	p-type thermoelectric leg
s	solid phase

Abbreviations

BTMS	battery thermal management system
CPCM	composite phase change material
COP	coefficient of performance
EG	expanded graphite
PW	paraffin wax
PCM	phase change material
TEC	thermoelectric cooler

latent heat capacity in a pure PCM may contribute to heat accumulation within the battery pack, surpassing the predefined temperature limit [11]. Consequently, multiple investigations have been carried out to augment the thermal conductivity of PCMs [12]. For instance, in the work by Ma et al. [13], where they crafted a composite phase change material (CPCM) using EG@Bi-MOF derived porous carbon/lauric acid for battery thermal management; The results showcase a notable 7.35-fold increase in the thermal conductivity of the CPCM compared to the pure PCM, and the enhancement enables efficient temperature control, especially during high-rate battery discharge. Wu et al. [14] performed a numerical investigation on the PCM-based BTMS, employing CPCM that consisted of paraffin waxes and different mass fractions of expanded graphite (EG); The findings revealed that achieving the optimal performance of the PCM-based BTMS was possible by utilizing a CPCM with an EG mass fraction ranging from 15 % to 20 %. The aforementioned studies successfully tackle the issue of low thermal conductivity in PCMs. Nevertheless, it is important to note that the latent heat capacity of PCMs remains constrained. Consequently, in scenarios involving high-rate discharge or challenging operational conditions, a singular PCM-based BTMS might fall short of fulfilling the thermal management requirements for batteries [15].

Given the capability of the air cooling method to extract latent heat from PCMs and shorten their melting time [16], numerous studies have focused on combining air cooling with PCMs to achieve effective battery thermal management. Ahmad et al. [17] conducted a numerical study on a BTMS, featuring fins embedded in PCMs coupled with air cooling; The findings revealed a substantial 18.6 % decrease in battery temperature, consistently keeping it below 313.15 K when compared to relying solely on air cooling. Yang et al. [18] performed a numerical investigation on a BTMS integrating PCMs with air cooling; The findings indicate that, under cyclic charging and discharging conditions, this combination exhibits superior thermal performance compared to using PCMs or air cooling individually, enabling the control of the maximum temperature of batteries within desirable limits. However, the efficiency of the air cooling method in dissipating heat is found to be low, limiting its ability to cool the interior of PCMs and only providing cooling for the

external surface of PCMs [19]. In comparison to air cooling, liquid cooling, characterized by higher thermal conductivity and specific heat, can effectively overcome the limitations associated with coupling PCMs to air cooling [20]. Rao et al. [21] developed a BTMS that incorporates micro-liquid cooling channels and PCMs; Through numerical simulations, they found that the developed BTMS could effectively adjust the battery temperature to below 320.6 K. Liu et al. [22] suggested a BTMS that integrates PCMs and a spiral liquid cooling tube, and conducted a comparative evaluation of its cooling performance with a BTMS using natural air cooling as the sole mechanism; The research findings indicate that, in comparison to natural air cooling, the developed BTMS achieved a cooling effect of 30 K. However, as the cooling demands for the BTMS become more exacting, it is crucial to develop advanced systems to fulfill the rapid cooling needs of batteries and prevent the excessive melting of PCMs [23].

Additionally, the development of BTMS must consider not only heat dissipation performance under high-temperature or high discharge rate conditions but also preheating performance in low-temperature environments [24]. However, achieving the preheating criteria for batteries at lower temperatures proves challenging for BTMS utilizing air or liquid cooling integrated with PCM [25]. Given the aforementioned shortcomings, the thermoelectric device, as a solid-state cooler, emerges as a promising technology to achieve effective thermal management for batteries due to its advantages of precise temperature control, bidirectional temperature regulation, and rapid temperature responses [26]. When the electrical current passes through the thermoelectric cooler (TEC), one end of the TEC will produce cooling power, and another end will produce heating power, due to the Peltier effect [27]. Additionally, the switching of the cooling and heating ends occurs when the direction of the input current changes. Therefore, a BTMS utilizing thermoelectric cooling can effectively meet both cooling demands in high-temperature conditions and preheating demands in low-temperature environments without the need for additional components like positive temperature coefficient elements. However, in the current studies concerning thermoelectric-based BTMS, the primary focus remains on examining their heat dissipation capabilities under standard operational conditions

[26,28], while insufficient attention is devoted to analyzing preheating effects in low-temperature environments and heat dissipation performance under conditions of elevated temperature or high discharge rates. Meanwhile, the relatively low thermal conductivity of pure PCMs used in current related research hinders the ability of TECs to effectively cool both batteries and PCMs. Additionally, regarding numerical models, prevailing research predominantly employs Computational Fluid Dynamics simulations or elementary analyses [29], lacking advanced numerical models that consider the intricate multi-physical field coupling phenomenon.

Based on this, to ensure the optimal operating temperature of the battery under challenging conditions such as high temperatures/high discharge rates and low-temperature environments, a BTMS integrating TEC, CPCMs, and liquid cooling is proposed, as described in Section 2. Additionally, a numerical model is constructed to accurately analyze the system's thermal performance, considering the multi-physics coupling phenomena of thermal, fluid, and electric fields, phase transition processes, and transient response characteristics. Section 3 gives a detailed introduction to the numerical model. Subsequently, Section 4 focuses on investigating the impact of critical parameters on the performance of the novel BTMS, including the EG mass fraction of CPCMs, TEC cooling input current, and coolant flow speed in the high-temperature situations, and the TEC preheating input current and ambient temperature in the low-temperature situations. Finally, Section 5 gives a summary of this work.

2. Geometric description of the BTMS

The proposed BTMS in this paper consists of five parts: the battery pack, a PCM framework, an aluminum framework, TECs, and two liquid cooling plates, as illustrated in Fig. 1. Eight 18650 lithium-ion battery units make up the battery pack. The PCM framework, with the

dimension of $42 \times 82 \times 65 \text{ mm}^3$, contains eight holes used to place eight battery units, and the space between holes is 2 mm. Paraffin wax and varying mass fractions of EG are combined to form the CPCMs used in the PCM framework. The aluminum framework measures $43 \times 83 \times 83 \text{ mm}^3$ in overall size and is characterized by a thickness of 0.5 mm. The PCM framework, embedded with eight battery units, is placed in the center of the aluminum frame. The aluminum frame is equipped with eight TECs, evenly distributed across its two side surfaces, with a 1 mm spacing between each TEC. The hot side of the TECs is equipped with a liquid cooling plate that features an interior flow channel in an S-shape, effectively dissipating heat. Specifically, the liquid cooling plate is characterized by a thickness of 6 mm, a flow channel diameter of 5 mm, and water serves as the coolant in the flow channel. Additionally, thermally silicone grease is applied to both sides of TECs to minimize contact thermal resistance and eliminate any air gaps.

Throughout the charging and discharging phases, the thermal energy emanating from batteries is stored as latent heat within the PCM. By activating the TEC with an electric current, the cooling power generated on its cold side is utilized to provide a low-temperature environment for both PCMs and batteries. This controlled cooling action slows down the melting process of PCMs, effectively preserving the maximum temperature of batteries within a reasonable operational range. Nonetheless, the inadequate thermal conductivity exhibited by pure PCMs imposes constraints on the efficiency of TECs in controlling the temperature of both the PCM and battery. The EG has high porosity, high surface activity, excellent thermal conductivity, and good compatibility with organic materials [32]; therefore, a CPCMs consisting of the EG and pure PCM is employed in this work to overcome the above challenges. Moreover, the cooling water circulating within the liquid cooling plates functions as a medium to absorb and dissipate the heat generated on the heating end of TECs. The three-dimensional geometry of the BTMS is created using Solidworks 2022 software. Detailed material parameters

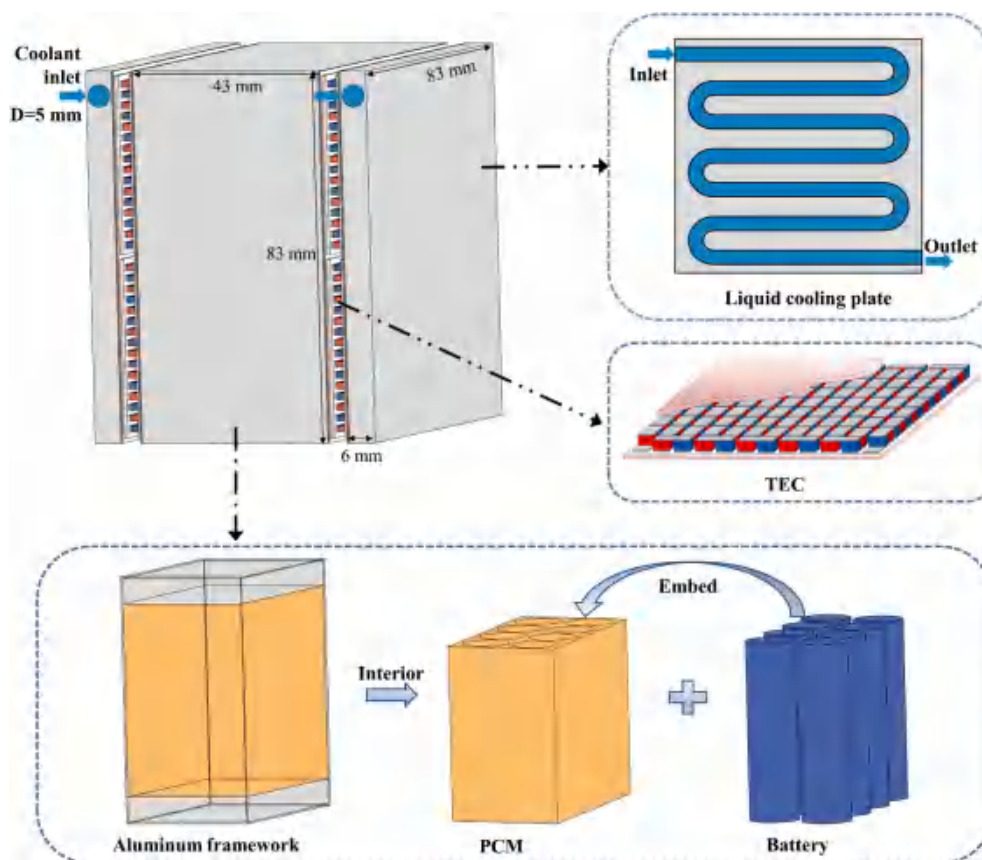


Fig. 1. Schematic diagram of the three-dimensional structure of the system.

Table 1

Detailed material parameters of the battery [30], aluminum, CPCMs [31], water, and thermal silicone grease [25].

Component	Thermal conductivity (W·m ⁻¹ ·K ⁻¹)	Density (kg·m ⁻³)	Specific heat (J·kg ⁻¹ ·K ⁻¹)	latent heat (J·kg ⁻¹)
Battery	x, y:1.07 z:19.03	2055.10	1129.95	–
Aluminum	238	2700	900	–
Water	0.62	998.20	4180	–
Thermal silicone grease	3	2600	1200	–
CPCMs:				
EG (0 %)/PW (100 %)	0.20	800	2000	255,000
EG (3 %)/PW (97 %)	0.58	825	1963	247,400
EG (6 %)/PW (94 %)	1.23	832	1926	239,700
EG (9 %)/PW (91 %)	3.50	845	1889	232,100
EG (12 %)/PW (88 %)	5.74	897	1852	224,400
EG (20 %)/PW (80 %)	10.1	913	1754	204,000

of the battery, aluminum, CPCM, water, and thermal silicone grease are shown in Table 1. The temperature range of the phase transition of CPCMs in this research is 314.15 K–317.15 K [31]. The material parameters for each component in the TEC are available in Table 2, given by Sagreon Corp. (Wuhan, China).

3. The numerical model of coupled multi-physics fields

Before conducting numerical simulations, it is necessary to make the following assumptions:

- (1) Heat generation within the battery is consistent and diffuses evenly in all orientations [33];
- (2) The battery electrodes are removed [34,35];
- (3) The thermophysical parameters of both the PCM and battery remain unchanging throughout the process [26];
- (4) The volume of PCM does not change on melting [26];
- (5) The effect of convective heat transfer after PCM melting is neglected [36,37].

3.1. Governing equations

Within the numerical model of coupled multi-physics fields, the governing equations are classified into three components: equations for the solid domain (excluding TECs), equations for the TEC domain, and equations characterizing the fluid domain.

3.1.1. The solid domain (excluding TECs)

For the solid domain of batteries, the energy conservation equation is articulated as:

$$\frac{\partial}{\partial t}(\rho_b c_{p,b} T_b) = \nabla \cdot (k_b \nabla T_b) + q_b \quad (1)$$

where, t represents the time, k and c_p are respectively the thermal conductivity and heat capacity, ρ and T are respectively the density and temperature, referring to the subscript b denotes the 18650 lithium-ion battery. q_b is the volume heat generation, which can be calculated by:

$$q_b = \frac{Q_b}{V_b} \quad (2)$$

where, Q_b is the heat source, V_b is the battery volume. The battery operates at a discharge rate of 5 C, at which juncture the precise value of Q_b can be referenced from Table 3 [30]. Besides, Table 4 presents the key parameters of the 18650 lithium-ion battery.

Within the solid domain of CPCMs, the enthalpy method is employed to elucidate the intricacies of the interior heat transfer mechanisms [26]:

$$\rho_{pcm} \frac{\partial H_{pcm}}{\partial t} = k_{pcm} \nabla^2 T_{pcm} \quad (3)$$

where, H_{pcm} are the enthalpy, with the subscript pcm indicating the phase change materials used in work. The enthalpy H_{pcm} is composed of two constituents, namely the sensible heat enthalpy h and the enthalpy of phase transition Δh :

$$h = \int_{T_0}^{T_{pcm}} c_{p,pcm} dT_{pcm} \quad (4)$$

$$\Delta h = \beta \gamma \quad (5)$$

$$H_{pcm} = h + \Delta h \quad (6)$$

where, β and γ are respectively the liquid fraction and latent heat. Here, the liquid fraction β is obtained through computation using the following equation:

$$\beta = \begin{cases} 0 & T_{pcm} < T_s \\ \frac{T - T_s}{T_l - T_s} T_l & T_l < T_{pcm} < T_s \\ 1 & T_{pcm} > T_l \end{cases} \quad (7)$$

where referring to subscripts l and s indicates the liquid and solid phases of CPCMs.

For the solid domain of the liquid cooling plate and aluminum framework, its governing equation can be expressed as:

$$\frac{\partial}{\partial t}(\rho_{al} c_{p,al} T_{al}) = \nabla \cdot (k_{al} \nabla T_{al}) \quad (8)$$

Table 2

Datasheet of the TEC.

Name	Seebeck coefficient ($\mu\text{V}\cdot\text{K}^{-1}$)	Thermal conductivity (W·m ⁻¹ ·K ⁻¹)	Electrical resistivity (10 ⁻⁵ Ω·m)	Size (L × W × H mm ³)
p-Type legs	$1.3222 \times 10^{-5} T^3 - 0.0171 T^2 + 7.3095 T - 853.6610$	$1.6848 \times 10^{-7} T^3 - 1.8949 \times 10^{-4} T^2 + 0.0697 T - 6.8387$	$-9.0350 \times 10^{-9} T^3 + 1.6380 \times 10^{-5} T^2 - 0.00425 T + 0.6648$	$1.4 \times 1.4 \times 1.6$
n-Type legs	$-1.5235 \times 10^{-5} T^3 + 0.0194 T^2 - 8.2297 T + 981.1090$	$1.4735 \times 10^{-7} T^3 - 1.5903 \times 10^{-4} T^2 + 0.0571 T - 5.0958$	$4.4520 \times 10^{-8} T^3 - 5.5288 \times 10^{-5} T^2 + 0.02591 T - 3.4085$	$1.4 \times 1.4 \times 1.6$
Copper electrodes	–	400	1.67×10^{-3}	$3.8 \times 1.4 \times 0.4$
Ceramic plates	–	22	–	$40 \times 40 \times 0.8$

Table 3
The Q_b of 18650 lithium-ion battery at 5 C discharge rate [30].

Time/s	0	71	144	216	287	360	432	504	576	648	720
Heat source/W	4.91	4.89	4.84	4.82	4.73	4.66	4.75	4.75	4.72	5.57	6.29

Table 4
Important parameters of the 18650 lithium-ion battery [30].

Parameter	Reference data
Rated capacity/mAh	2000
Weight/g	45 ± 1
Internal resistance/mΩ	45
Max charge voltage/V	4.2
End-off voltage/V	2.7
Voltage rating/V	3.7
I _{max} /A	10
Maximum charging current/A	2

3.1.2. The TEC domain

All components within the TEC are subject to adherence to the energy conservation equation [38]:

$$\frac{\partial}{\partial t}(\rho_m c_{p,m} T_m) = \nabla \cdot (k_m \nabla T_m) + S_m \quad (9)$$

with

$$\dot{S}_m = \begin{cases} \sigma_n^{-1}(T) \vec{J}^2 - T_n \vec{J}^{-1} \cdot \nabla \alpha_n(T) - \frac{\partial \alpha_n(T)}{\partial T} T \vec{J} \cdot \nabla T_n; & \text{n-type thermoelectric leg (10-1)} \\ \sigma_p^{-1}(T) \vec{J}^2 - T_p \vec{J}^{-1} \cdot \nabla \alpha_p(T) - \frac{\partial \alpha_p(T)}{\partial T} T \vec{J} \cdot \nabla T_p; & \text{p-type thermoelectric leg (10-2)} \\ 0; & \text{ceramic (10-3)} \\ \sigma_{co}^{-1}(T) \vec{J}^2; & \text{copper electrode (10-4)} \end{cases} \quad (10)$$

where, the subscripts m, p, n, co, and ce are used to represent distinct materials: m for different material name, p for p-type thermoelectric leg, n for n-type thermoelectric leg, co for copper electrode, and ce for ceramic plate. The term \dot{S}_m denotes the energy source, σ^{-1} denotes the inverse electrical resistivity, \vec{J} denotes the current density vector, and α denotes the Seebeck coefficient.

The governing equation of the electric field holds true for both p- and n-type thermoelectric legs and both copper electrodes in the TEC [39]:

$$\vec{E} = -\nabla \phi + \alpha_{p,n}(T) \nabla T \quad (11)$$

$$\vec{J} = \sigma_m \vec{E} \quad (12)$$

$$\nabla \cdot \vec{J} = 0 \quad (13)$$

where, ϕ and \vec{E} are the electric potential and electric field density vector respectively.

3.1.3. The fluid domain

The coolant in the fluid domain follows the basic equations of the computational fluid dynamics theory [40,41]:

$$\frac{\partial}{\partial t}(\rho c_p T) + \nabla \cdot (\rho c_p \vec{v} T) = \nabla \cdot (k \nabla T) \quad (14)$$

$$\frac{\partial}{\partial t}(\rho \vec{v}) + \nabla \cdot (\rho \vec{v} \vec{v}) = -\nabla p + \nabla \cdot (\mu \nabla \vec{v}) \quad (15)$$

$$\frac{\partial \rho}{\partial t} + \nabla \cdot (\rho \vec{v}) = 0 \quad (16)$$

where \vec{v} and μ are respectively the velocity vector of coolant and dynamic viscosity. The specific flow pattern of the coolant is determined by its Reynolds number, which can be calculated by

$$Re = \frac{\rho v d}{\mu} \quad (17)$$

where, d and v are respectively the hydraulic diameter and coolant flow speed. The simulations in this study utilize the laminar model, attributing to the fact that the maximum coolant flow speed does not surpass 0.1 m/s and the Reynolds number is below 2000 [42].

3.2. Boundary conditions

This work simulates the proposed numerical model of coupled multi-physics fields using COMSOL Multiphysics 6.0 software. To assess the cooling efficiency of the system under extreme conditions, characterized

by both high temperature and high discharge rates, the discharge rate of the 18650 lithium-ion battery is specified at 5C for a duration of 720 s, while maintaining the ambient temperature at 313.15 K. For the boundary condition of the TEC, one side is defined as the current inlet (cooling input current), and another side is set to be grounded. A velocity inlet with a water temperature of 313.15 K is designated at the inlet surface of the coolant channel in the liquid cooling plate, while a pressure outlet is established at the outlet surface of the water channel, set to atmospheric pressure. During the preheating performance simulation, the liquid cooling plate does not operate; The current direction of the TEC is opposite to that used for the cooling performance simulation, and thus, the original grounded boundary condition is set as a current inlet (preheating input current) boundary condition herein, and vice versa; Besides, other boundary conditions keep the same as those during the cooling performance simulation. In simulations assessing both cooling and preheating performance, a natural convection boundary condition is imposed on the surfaces of the BTMS interacting with the environment, as follows:

$$-k \frac{\partial T}{\partial n} = h_{am}(T - T_{am}) \quad (18)$$

where $h = 5 \text{ W} \cdot \text{m}^{-2} \cdot \text{K}^{-1}$ represents the natural convective heat transfer coefficient, and the subscript am denotes the ambient conditions.

3.3. Parameter definition

The thermal performance of the TEC is assessed using two crucial parameters: cooling power (Q_c) and coefficient of performance (COP).

Upon applying the input current to the TEC, the heat absorbed by the cold end is denoted as Q_c , while the heat released at the heating end is represented as Q_h [28]:

$$Q_c = \alpha I_{TEC} T_c - 0.5 I_{TEC}^2 R_{TEC} - k_{TEC} (T_h - T_c) \quad (19)$$

$$Q_h = \alpha I_{TEC} T_h + 0.5 I_{TEC}^2 R_{TEC} - k_{TEC} (T_h - T_c) \quad (20)$$

where, α and k_{TEC} are respectively the Seebeck coefficient and thermal conductivity, T_c and T_h are respectively the cooling end temperature and heating end temperature, R_{TEC} and I_{TEC} are respectively the resistance and input current of the TEC [28].

Combining Eqs. (19) and (20), the TEC input power can be expressed as:

$$P = Q_h - Q_c = I_{TEC}^2 R_{TEC} + \alpha I_{TEC} (T_h - T_c) \quad (21)$$

Therefore, the COP of the TEC can be defined by:

$$COP = \frac{Q_c}{P} \quad (22)$$

3.4. Grid independence examination

To ensure the accuracy of numerical simulations and minimize computational costs, it is imperative to conduct a grid independence examination. In this section, the numerical simulation for the BTMS with pure PW-based PCMs is performed, with the TEC cooling input current set at 3 A and the coolant flow speed at 0.1 m/s. Moreover, four grid cases are employed to verify the grid independence, comprising 286172, 585390, 1226991, and 2686269 grid numbers. Fig. 2 illustrates that the grid number minimally impacts the maximum battery temperature when exceeding 1226991. Consequently, the case with 1226991 grid numbers is chosen for subsequent studies, taking into account the trade-off between calculation accuracy and computational resources.

3.5. Experimental validation

The prototype of the BTMS is currently in the manufacturing process, but it is time-consuming. Therefore, to ensure the accuracy of the developed numerical model, experimental data from Ref. [28] is compared with the numerical results obtained from the proposed model, where the BTMS is composed of batteries, TECs, PCMs, and liquid cooling devices. Based on this, the geometric structure of the BTMS, as detailed in Ref. [28], is reconstructed, and numerical simulations are conducted using the developed numerical model. It is crucial to emphasize that the boundary conditions employed during the simulation align with the experimental conditions. Fig. 3 depicts a comparison between the numerical results and the experimental data. Notably, the numerical simulation yields results and trends that closely match the experimental data from Ref. [28], with an average absolute error of the maximum temperature of only 0.92 K over a 7200 s. The outcomes reveal that the constructed numerical model is proficient in accurately assessing the system's thermal performance, thereby augmenting the rationality and reliability of the subsequent research efforts to a certain extent.

4. Results and discussion

This study examines the thermal performance of the system under extreme operational conditions, focusing on two aspects: cooling performance under high-temperature/high-discharge-rate conditions and preheating performance under low-temperature conditions. Within the analysis of cooling performance, this study explores the influence of various CPCMs, TEC cooling input currents, and inlet flow speeds. Simultaneously, in the analysis of preheating performance, the study examines the influence of TEC preheating input currents and ambient temperatures.

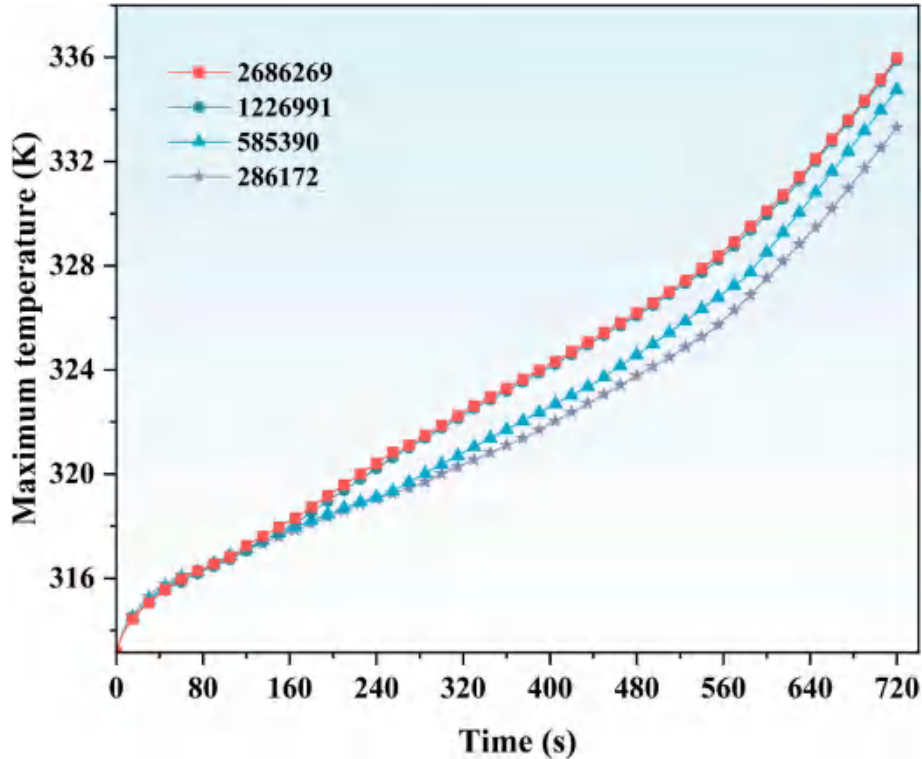


Fig. 2. Effect of different numbers of grids on maximum battery temperature.

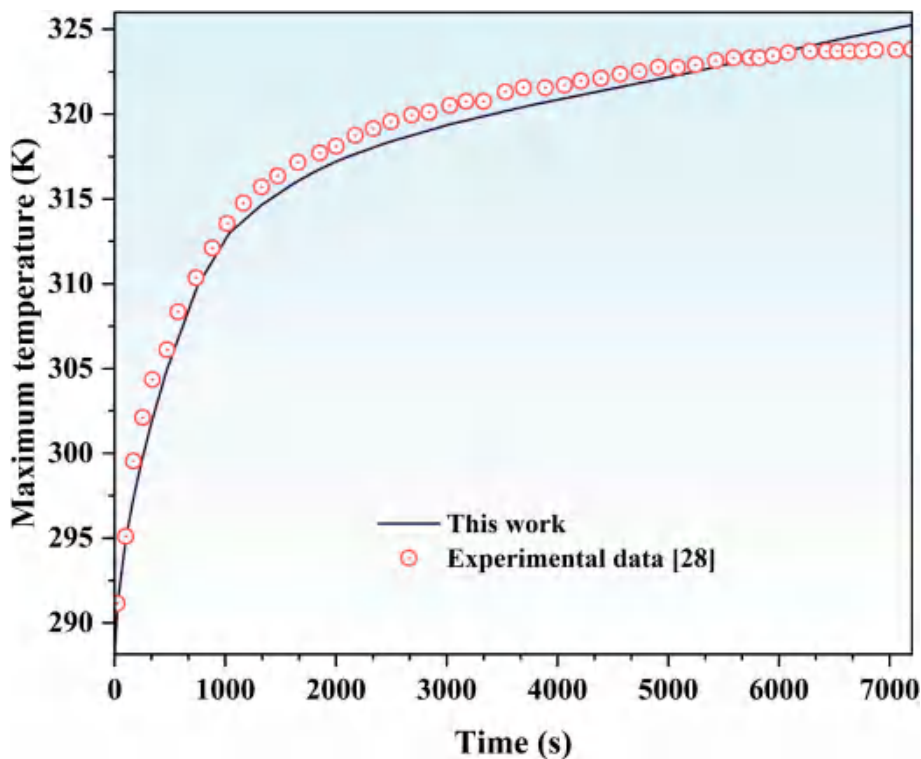


Fig. 3. Comparison of the maximum temperature between numerical results and experimental results.

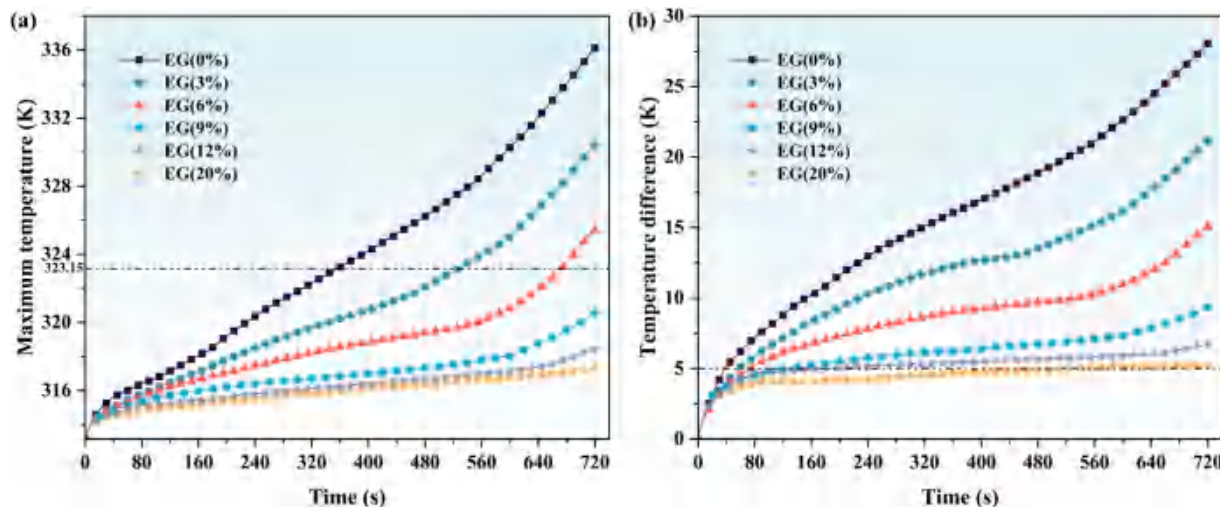


Fig. 4. The influence of CPCMs with different mass fractions of EG on the cooling performance. (a) Maximum temperature; (b) Temperature difference among batteries.

4.1. Influence of different EG mass fractions of CPCMs on the cooling performance

The system’s cooling performance is analyzed in this section by considering various EG mass fractions of CPCMs: 0 %, 3 %, 6 %, 9 %, 12 %, and 20 %. The TEC cooling input current and coolant flow speed are held constant at 3 A and 0.1 m/s, respectively. Fig. 4(a) presents the variations in the maximum temperature of batteries, and Fig. 4(b) demonstrates the changes in the temperature difference among batteries. With an increase in the EG mass fraction, the thermal conductivity of CPCMs rises, allowing the TEC to supply lower temperatures to both CPCMs and batteries, leading to a decrease in both the temperature difference and maximum temperature. When the EG mass fraction is set

at 20 %, the temperature difference and maximum temperature are the lowest at 5.21 K and 317.33 K, respectively. Notably, compared to pure PW-based CPCMs without EG, this configuration results in a decrease of 22.84 K and 18.81 K in the temperature difference and maximum temperature, respectively. Additionally, it is observed that for EG mass fractions of 0 %, 3 %, 6 %, and 9 %, the temperature difference and maximum temperature experience a rapid increase during the later stages of the discharging process. In this situation, the thermal conductivity of CPCMs is reduced due to the decrease in EG mass fraction, which weakens the ability of TECs to dissipate heat accumulated at the center of CPCMs, therefore, the melting in that region of CPCMs causes notable rises in the temperature difference and maximum temperature. However, at the EG mass fractions of 12 % and 20 %, a higher thermal

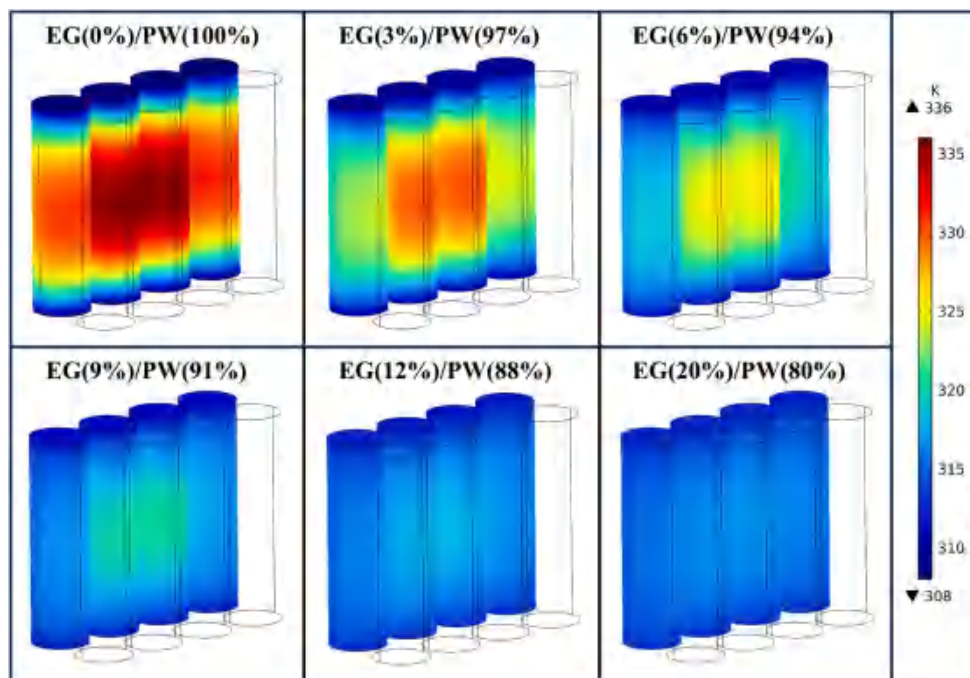


Fig. 5. Battery temperature contours at 720 s for various EG mass fractions.

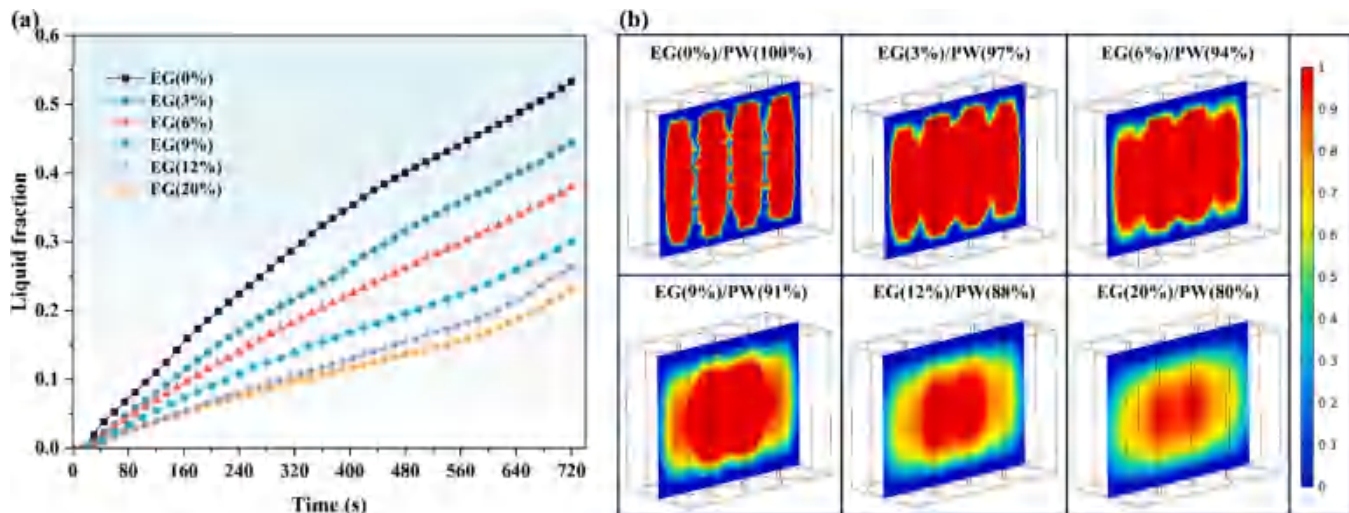


Fig. 6. Liquid fraction of CPCMs under various EG mass fractions. (a) The fluctuation of liquid fraction as the undergoes discharge; (b) Countors of the liquid fraction distribution at the intermediate cross-section of CPCMs at 720 s.

conductivity of CPCMs allows for more efficient cooling by the TEC, preventing a significant increase in the temperature difference and maximum temperature.

Fig. 5 demonstrates the contour of the internal temperature distribution of the battery pack at 720 s. It can be found that the center of the battery pack has the highest temperature. By increasing the EG mass fraction, corresponding to an improvement in the thermal conductivity of the CPCM, an effective reduction is achieved in both the temperature difference and maximum temperature of batteries. At the EG mass fraction is low, a significant temperature gradient is observed in batteries, which is due to the high thermal conductivity of the aluminum frame allowing TEC cooling power to be effectively transmitted to the top and bottom of the battery pack, while the large thermal resistance of CPCMs limits its transmission to the interior of batteries. At EG mass fractions of 12 % and 20 %, a substantial reduction in the maximum

temperature is observed, alongside a more uniform surface temperature of the battery, indicating the elimination of the large temperature difference phenomenon and an advancement in battery temperature uniformity.

The variation of the liquid fraction as the discharge proceeds is depicted in Fig. 6(a). In the situation of an EG mass fraction of 20 %, the liquid fraction of CPCMs reaches 0.230 at 720 s, showing a reduction of 0.302 compared to pure PW-based CPCMs without EG. This is attributed to the heightened thermal conductivity of the CPCM, which improves the heat transfer from TEC to CPCM, subsequently diminishing the melting rate of CPCM. More details about the liquid fraction distribution can be found in Fig. 6(b). At low EG mass fractions, the CPCM near the battery area melts while other areas remain unchanged, primarily due to the limited heat dissipation caused by the low thermal conductivity of CPCMs. As the mass fraction of EG increases, the improved thermal

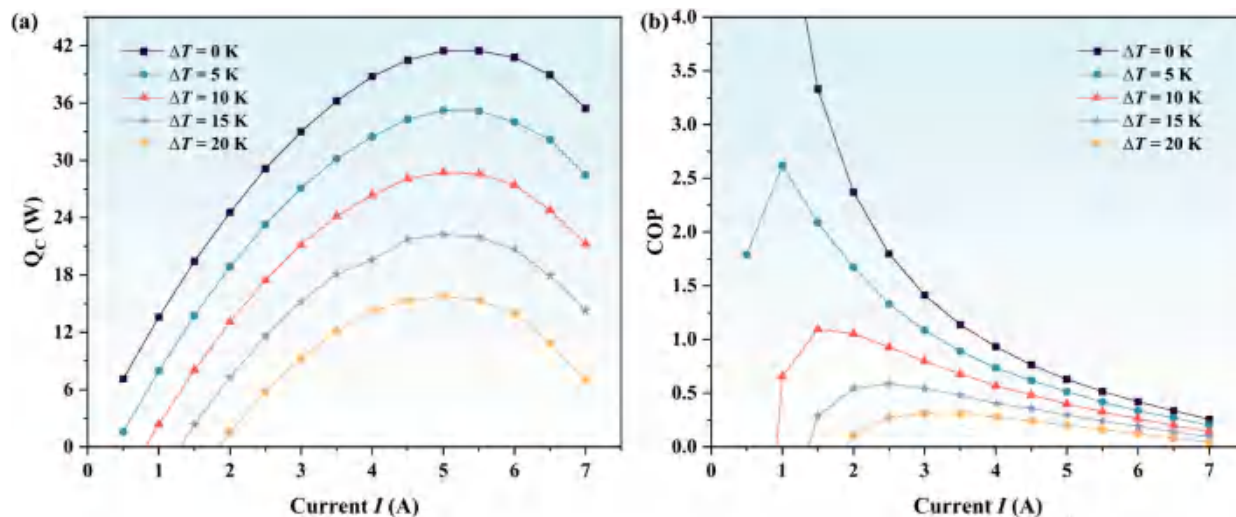


Fig. 7. TEC cooling performance under various working conditions. (a) Cooling power; (b) COP.

conductivity of CPCMs facilitates effective heat transfer from batteries to CPCMs, resulting in a noticeable color gradient in the melting area of CPCMs. Additionally, the melting of the central region of CPCMs restricts its heat absorption capacity from batteries, leading to a significant increase in both the temperature difference and maximum temperature during the later phases of battery discharge.

Through the above analysis, it is determined that the BTMS exhibits optimal cooling performance at EG mass fractions of 12 % and 20 %. However, higher EG mass fractions result in lower latent heat of CPCMs and increased material instability [43]. Therefore, the EG mass fraction of 12 % is selected for subsequent research.

4.2. Influence of the TEC cooling input current on the cooling performance

Before exploring how the TEC cooling input current affects the system's cooling performance, it is crucial to establish the appropriate range for the TEC working current. Therefore, numerical simulations for the TEC are conducted to study its cooling power and COP under different temperature differences and input currents. The variation of cooling power and COP with different temperature differences and input currents are respectively presented in Fig. 7(a) and (b). Under constant input current, both the cooling power and COP of the TEC diminish with

an increase in temperature difference. Therefore, it is imperative to implement effective cooling at the heating end of the TEC to guarantee optimal cooling performance. In addition, there is a trend of initial augmentation and subsequent reduction in the cooling power and COP of the TEC as the input current is raised. The highest cooling power is obtained when the current is 5 A, while the peak COP occurs at a lower input current value and is particularly sensitive to the TEC's temperature difference. Clearly, the TEC's cooling performance diminishes when the input current surpasses 5 A. Therefore, the range of 1 A to 5 A is selected to investigate the effect of TEC cooling input current on the cooling performance of the BTMS.

Fig. 8(a) presents the variations in the maximum temperature of batteries, and Fig. 8(b) demonstrates the changes in the temperature difference among batteries. As the TEC cooling input current increases, the maximum temperature gradually decreases, while the temperature difference increases accordingly. Employing a 5 A TEC input current results in a 7 K reduction in the maximum temperature to 315.95 K compared to a 1 A input current. Nevertheless, the temperature difference shows a consistent rise in conjunction with the increase in cooling input current, peaking at 10.63 K when the input current is set at 5 A. This phenomenon can be ascribed to the heightened cooling power of TECs, resulting in a rapid reduction in the surface temperature of batteries adjacent to TECs, thus exacerbating the non-uniformity of the

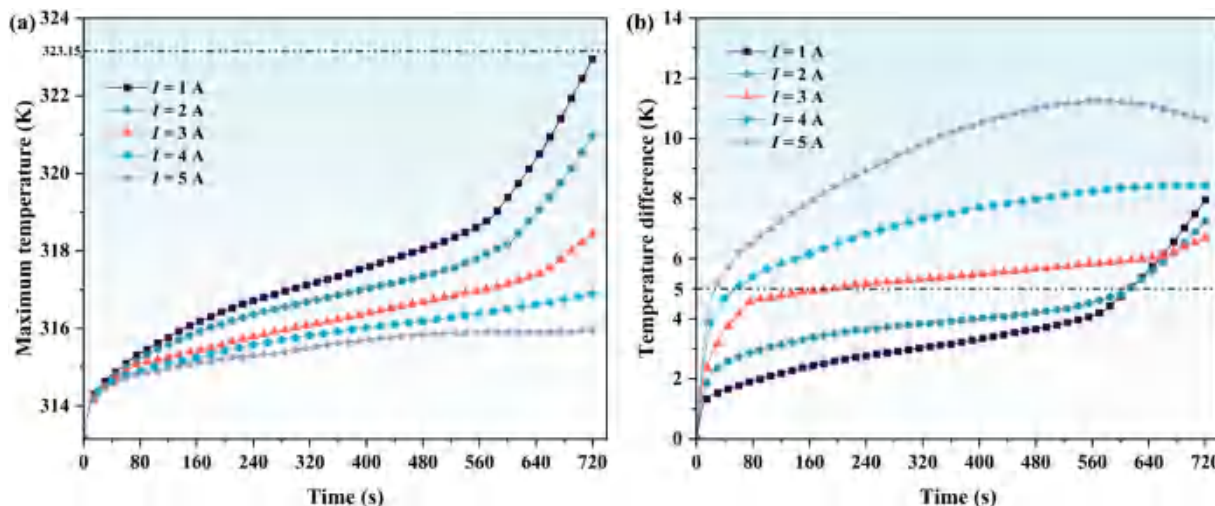


Fig. 8. The influence of the TEC cooling input current on the cooling performance. (a) Maximum temperature; (b) Temperature difference among batteries.

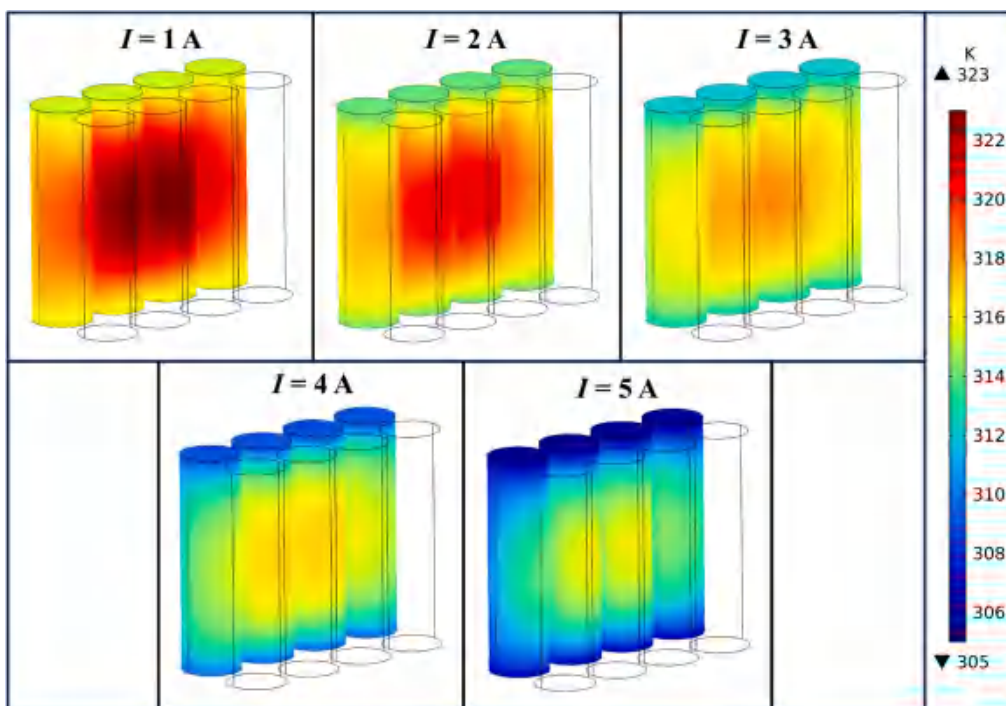


Fig. 9. Battery temperature contours at 720 s for various TEC cooling input currents.

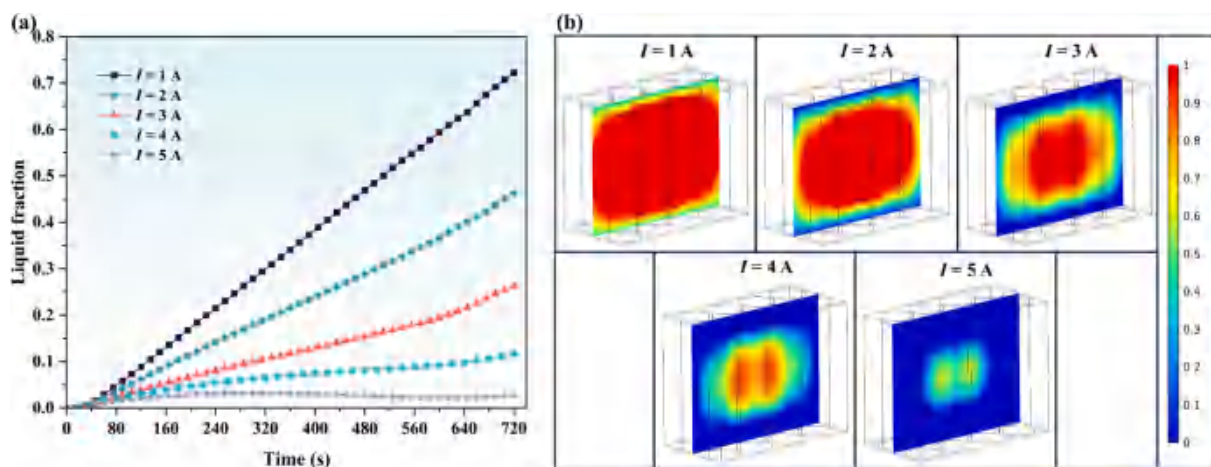


Fig. 10. Liquid fraction of CPCMs under various cooling input currents. (a) Variation of liquid fraction during discharge; (b) Contours of the liquid fraction at the intermediate cross-section of CPCMs at 720 s.

battery temperature. Moreover, at cooling input currents of 1 A or 2 A, the temperature difference and maximum temperature, although initially within acceptable limits for most of the discharge duration, undergo rapid escalation beyond these limits at 570 s and 600 s, respectively. This phenomenon is attributed to the comparatively low cooling power of the TEC, resulting in the complete melting of CPCMs and subsequent loss of cooling capacity.

Fig. 9 displays the temperature distribution contours within the battery pack at 720 s. Obviously, as the center of the battery pack is farther away from the TEC, the heat accumulated can not be effectively dissipated, resulting in the highest temperature. Increasing the input current of the TEC enhances its cooling capacity, allowing for more efficient cooling of the high-temperature regions within the CPCM and battery pack, ultimately eliminating the elevated temperatures in these areas.

The variation of the CPCM liquid fraction for various cooling input

currents is illustrated in Fig. 10(a). As the cooling input current increases, the liquid fraction of CPCMs decreases. At the end of the discharge, the CPCM liquid fraction is 0.027 at a cooling input current of 5 A, a decrease of 0.695 compared to a current of 1 A. At a cooling input current of 1 A, the CPCM undergoes considerable melting, except for the portion adjoining the aluminum framework, as visually represented in Fig. 10(b). As the cooling input current increases, the molten region of CPCMs diminishes progressively toward the center. Additionally, at a cooling input current of 5 A, the CPCM exhibits minimal melting.

According to the above analysis, the cooling input current of 3 A is selected as the optimum value to balance the temperature difference and maximum temperature within acceptable limits and minimize the TEC power consumption.

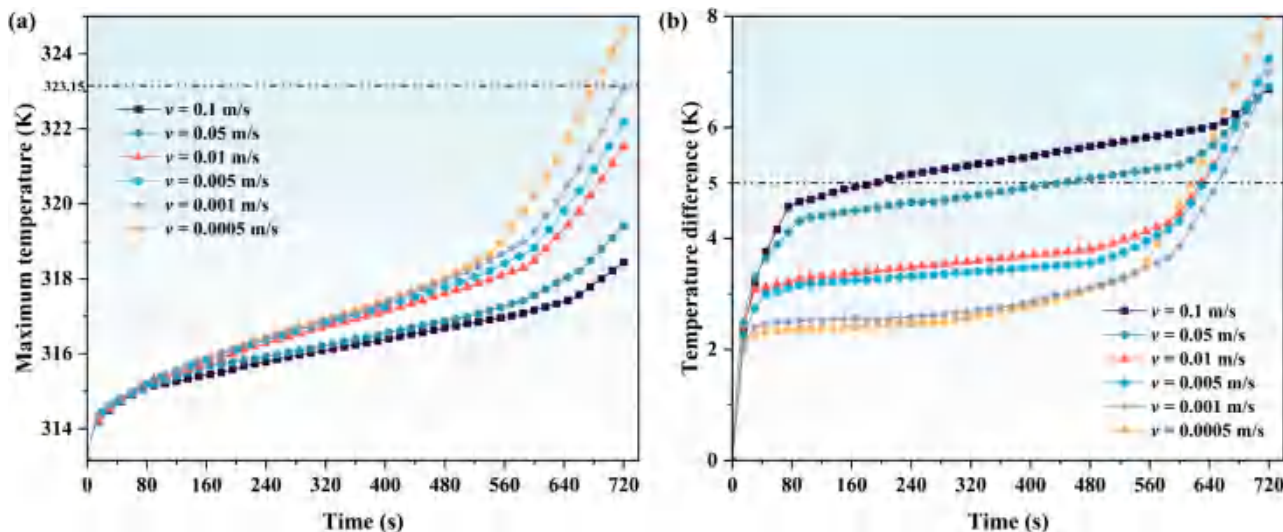


Fig. 11. The influence of the coolant flow speed on the cooling performance. (a) Maximum temperature; (b) Temperature difference among batteries.

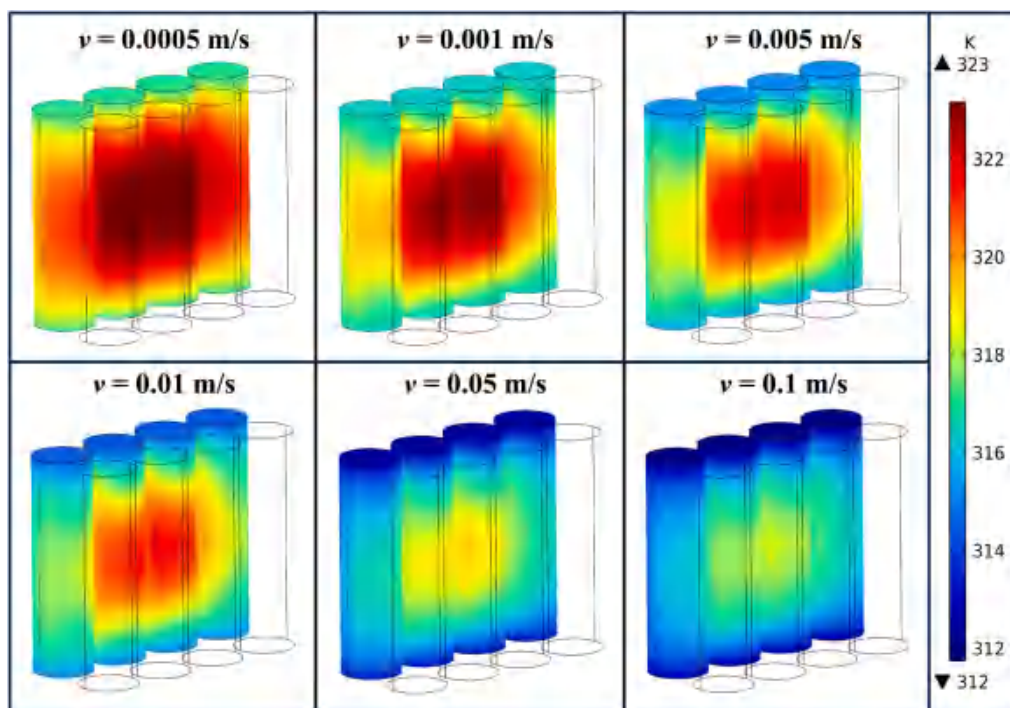


Fig. 12. Battery temperature contours at 720 s for various coolant flow speeds at 720 s.

4.3. Influence of the coolant flow speed on the cooling performance

Numerical simulations of the TEC demonstrate that high temperatures at the heating end result in a reduction in both the COP and cooling power of the TEC. Despite the efficient temperature regulation provided by the liquid cooling plate, a higher coolant flow speed can result in substantial energy consumption. Therefore, the identification of an optimal coolant flow speed is integral for the purpose of minimizing energy consumption in the BTMS. Fig. 11(a) presents the variations in the maximum temperature of batteries, and Fig. 11(b) demonstrates the changes in the temperature difference among batteries. The maximum temperature exhibits an upward trend, whereas the temperature difference exhibits a downward trend as the coolant flow speed decreases. This is due to the fact that the reduced coolant flow rate causes the temperature at the heating end of the TEC to increase, which worsens

the TEC's cooling performance. With a coolant flow speed of 0.1 m/s, the maximum temperature is recorded at 318.44 K, demonstrating a decrease of 6.15 K in comparison to the condition observed at a coolant flow speed of 0.0005 m/s. It is worth noting that a coolant flow speed below 0.001 m/s will cause the maximum temperature to surpass 323.15 K. As a result, to maintain the maximum temperature within an appropriate operational temperature range, it is advisable to set the coolant flow speed above 0.001 m/s. Besides, a relatively low coolant flow speed is insufficient to prevent the melting of CPCMs, resulting in a notable and swift escalation of both the maximum temperature and temperature difference during the later stages of the discharging process.

More details about the temperature distribution inside the battery pack can be gained from Fig. 12. Similarly, the interior of the battery pack experiences its highest temperature in the middle region. A

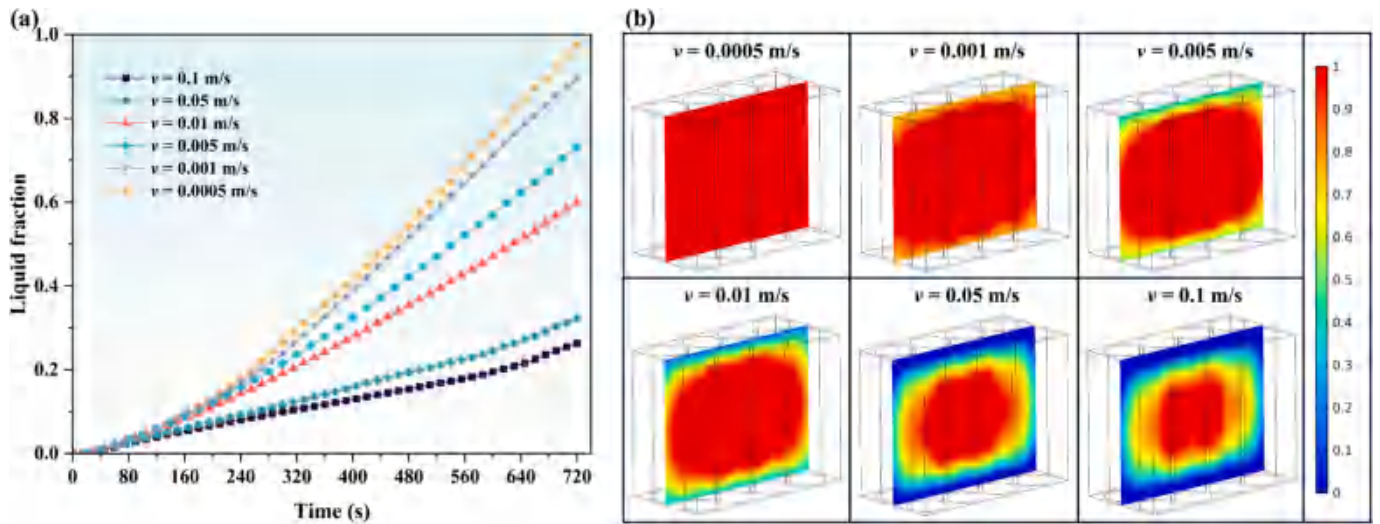


Fig. 13. Liquid fraction of CPCMs under various coolant flow speeds. (a) Variation of liquid fraction during discharge; (b) Contours of the liquid fraction at the intermediate cross-section of CPCMs at 720 s.

discernible reduction in the maximum temperature of the batteries is evident with an increase in coolant flow speed. Nevertheless, as the coolant flow speed goes beyond 0.05 m/s, the effects on the temperature difference and maximum temperature of batteries become progressively less significant with the incremental increase in coolant flow speed. Therefore, a coolant flow speed of 0.05 m/s seems to be the favored option.

The variation of the CPCM liquid fraction for various coolant flow speeds is illustrated in Fig. 13(a). The reduction of coolant flow speed results in an increase in the liquid fraction of CPCMs, and its effect is more significant compared to the maximum temperature and temperature difference. The liquid fraction of CPCMs experiences a significant upswing to 0.974 at 720 s under a coolant flow speed of 0.0005 m/s, surpassing the value at 0.1 m/s by 0.711. At coolant flow speeds of 0.001 m/s and 0.0005 m/s, CPCMs are almost completely melted, as shown in Fig. 13(b). In addition, with an increase in coolant flow speed, the melted area of CPCMs gradually shifts toward the center. After surpassing 0.05 m/s, the impact of raising the coolant flow speed on the liquid fraction of CPCMs becomes less pronounced. Consequently, the optimal coolant flow speed suggested in this investigation is 0.05 m/s.

4.4. Influence of the TEC preheating input current on the preheating performance

By reversing the input current direction, the TEC can effectively switch the positions of its hot and cold sides, offering a distinctive mechanism that enables the preheating of batteries in low-temperature environments without requiring supplementary heating equipment. The present section focuses on studying the system's preheating performance under various TEC preheating input currents (ranging from 1 A to 5 A). The evaluation is conducted using a CPCM of 12 % EG mass fraction and an ambient temperature of 263.15 K, while disregarding the coolant channel.

Fig. 14(a) demonstrates the variation of the minimum battery temperature for various TEC preheating input currents. It can be seen that the higher the TEC preheating input current, the faster the minimum temperature increases. Under a preheating input current of 5 A, the system attains a minimum temperature of 293.15 K in just 2240 s, a marked improvement over the 5600 s needed at 4 A. Notably, the preheating of the battery to 293.15 K is unachievable with a preheat input current less than 3 A. Besides, the temperature difference shows an

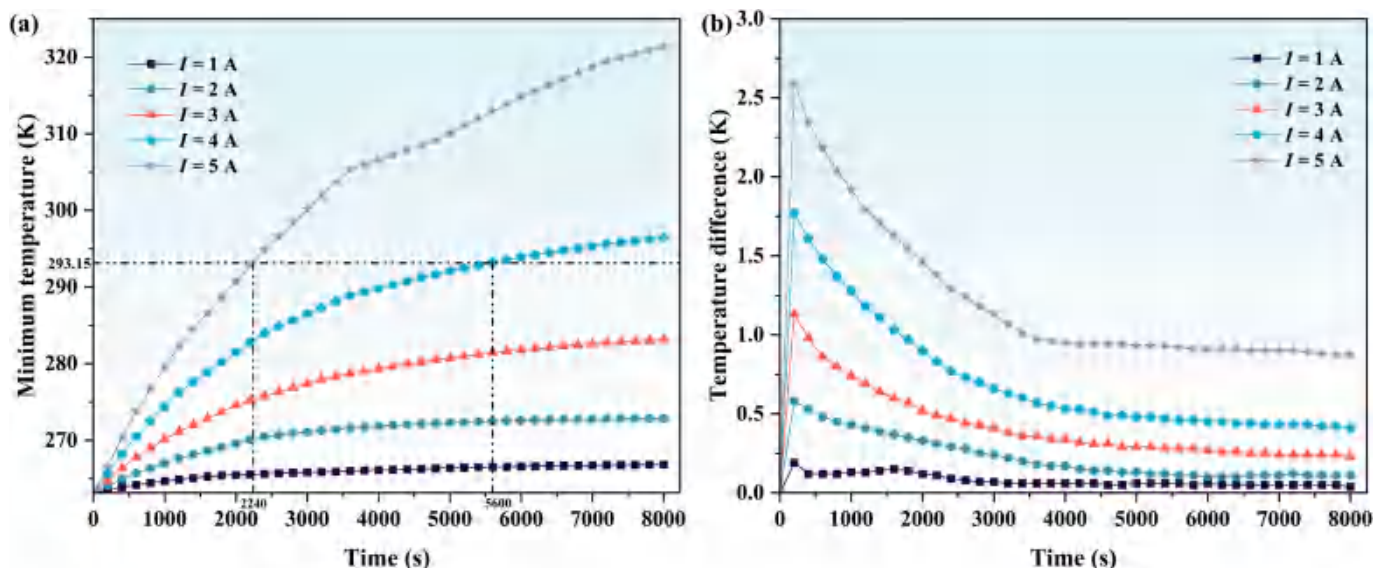


Fig. 14. The influence of the TEC preheating input current on the preheating performance. (a) minimum temperature; (b) Temperature difference.

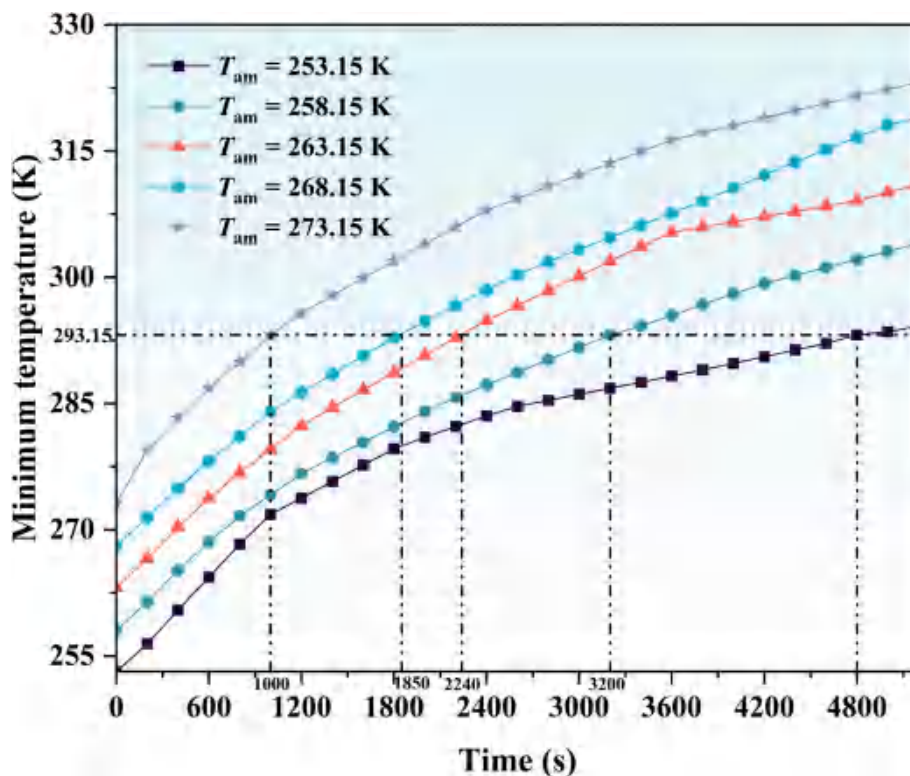


Fig. 15. The influence of ambient temperature on the preheating performance.

upward trend as the TEC preheating input current rises, as indicated in Fig. 14(b). Throughout the preheating phase, the temperature difference experiences an initial rapid escalation followed by a subsequent decrease, ultimately reaching a stabilized state. This is because the TEC responds immediately after the current is applied, and the battery surfaces close to the TEC are heated first, but the interior of the battery is not yet heated. With the increase in preheating time, the heat gradually transfers to the interior of the battery pack, making the temperature difference eventually maintained at a fixed value. Under the TEC preheating input current of 5 A, the battery pack shows the highest temperature difference of 2.59 K, indicating high temperature uniformity, which is beneficial for the normal start of the battery after preheating. Additionally, a fraction of the heat generated by the TEC while preheating is stored as latent heat within the CPCMs. Accordingly, the preheating input current of 5 A is suggested for the proposed BTMS to reduce the battery preheating time and adapt to more severe low-temperature environments.

4.5. Influence of the ambient temperature on the preheating performance

Fig. 15 illustrates the influence of ambient temperature on the preheating performance under the preheating input current of 5 A. The prolongation of the duration needed to elevate the battery pack's minimum temperature to 293.15 K is evident with decreasing ambient temperatures, as demonstrated in the results. At an ambient temperature of 273.15 K, the battery pack reaches a minimum temperature of 293.15 K within a 1000 s interval. However, when the ambient temperature drops to 253.15 K, the time needed for the minimum temperature to reach the same level increases significantly to 4800 s. Also, it can be obtained that even in a low-temperature environment of 253.15 K, the TEC preheating input current of 5 A can still meet the preheating performance requirements of the BTMS. It is noteworthy that the temperature difference of the battery pack exhibits negligible changes in response to variations in ambient temperature, and hence, it is not explicitly presented in this analysis.

5. Conclusions

To address the temperature challenges faced by batteries under extreme operating conditions, a novel BTMS solution is introduced, incorporating TECs and CPCMs to achieve precise temperature regulation. Meanwhile, considering the multi-physical coupling phenomenon of the thermal, fluid, and electric fields, a numerical model is constructed to accurately analyze the system's thermal performance. Under high temperature/high discharge rate conditions, the effect of the EG mass fraction of CPCMs, TEC cooling input current, and coolant flow speed on the cooling performance of the novel BTMS are comprehensively studied. In a similar vein, the comprehensive analysis of the TEC preheating input current and ambient temperature on the preheating performance of the novel BTMS is conducted under low-temperature conditions. The primary conclusions are as follows:

- (1) Increasing the EG mass fraction of CPCMs results in a decrease in the temperature difference and maximum temperature of batteries, along with a corresponding decline in the liquid fraction of CPCMs. To balance the cooling performance and effectiveness of CPCMs, an EG mass fraction of 12 % for CPCMs is suggested. Specifically, compared to pure PW-based CPCMs without EG, when the EG mass fraction is 12 %, the maximum temperature and temperature difference decrease by 17.70 K and 21.36 K, respectively, and the liquid fraction of CPCMs decreases by 0.273.
- (2) The TEC cooling input current has a parabolic relationship with both the cooling power and COP, increasing first and then decreasing. To achieve optimal performance, it is recommended to keep the current below 5 A. Additionally, as the input current rises, the maximum temperature gradually decreases, while the temperature difference increases proportionally. By utilizing the cooling input current of 3 A, the temperature difference and maximum temperature of batteries can be maintained at

reasonable levels, not exceeding 6.69 K and 318.36 K, respectively.

- (3) The liquid fraction of CPCM and the maximum temperature of the battery pack exhibit a gradual decrease as the coolant flow rate increases, while the temperature difference experiences an increase. A coolant flow speed of 0.05 m/s is suggested to balance the cooling performance and power consumption. When the coolant flow speed is 0.05 m/s, the maximum temperature and temperature difference and CPCM liquid fraction remain within reasonable limits, with maximum values of 319.40 K, 6.73 K, and 0.322, respectively.
- (4) The time required for the minimum battery temperature to reach 293.15 K exhibits a substantial decrease with an escalating TEC preheat input current. At a preheating input current of 5 A, it takes 2240 s for the battery to reach the minimum temperature of 293.15 K, while the battery can not be heated to 293.15 K when the current is less than 3 A. As the ambient temperature decreases, the preheating time for the battery pack increases, reaching 4800 s at an ambient temperature of 253.15 K.

CRedit authorship contribution statement

Ding Luo: Writing – original draft, Supervision, Methodology, Conceptualization. **Zihao Wu:** Writing – original draft, Visualization, Validation, Data curation. **Yuying Yan:** Writing – review & editing. **Zeyu Sun:** Resources, Funding acquisition. **Lin Yang:** Writing – review & editing. **Bingyang Cao:** Writing – review & editing, Project administration, Funding acquisition.

Declaration of competing interest

We declare that we do not have any commercial or associative interest that represents a conflict of interest in connection with the work submitted.

Data availability

Data will be made available on request.

Acknowledgements

This work was supported by the National Natural Science Foundation of China (Grant Nos. 52306017, U20A20301, 52250273), the Natural Science Foundation of Hubei Province (No. 2023AFB093), and the Key Laboratory of Modern Agricultural Equipment and Technology (Jiangsu University), Ministry of Education (MAET202310).

References

- [1] J. Cao, J. Wu, H. Wu, Y. Jin, D. Luo, X. Yang, et al., Dendrite-free zinc anode via oriented plating with alkaline earth metal ion additives, *Adv. Funct. Mater.* (2024) 2401537.
- [2] J. Niu, N. Xie, Y. Zhong, X. Gao, Y. Fang, Z. Zhang, Numerical analysis of battery thermal management system coupling with low-thermal-conductive phase change material and liquid cooling, *J. Energy Storage* 39 (2021) 102605.
- [3] D. Luo, Y. Zhao, J. Cao, W.-H. Chen, Y. Zhao, B. Cao, Performance analysis of a novel thermoelectric-based battery thermal management system, *Renew. Energy* 224 (2024) 120193.
- [4] P. Ping, Y. Zhang, D. Kong, J. Du, Investigation on battery thermal management system combining phase changed material and liquid cooling considering non-uniform heat generation of battery, *J. Energy Storage* 36 (2021) 102448.
- [5] G. Cheng, Z. Wang, X. Wang, Y. He, All-climate thermal management structure for batteries based on expanded graphite/polymer composite phase change material with a high thermal and electrical conductivity, *Appl. Energy* 322 (2022) 119509.
- [6] D. Luo, Z. Wu, L. Jiang, Y. Yan, W.-H. Chen, J. Cao, et al., Realizing rapid cooling and latent heat recovery in the thermoelectric-based battery thermal management system at high temperatures, *Appl. Energy* 370 (2024) 123642.
- [7] M. Faizan, S. Pati, P. Randive, Implications of novel cold plate design with hybrid cooling on thermal management of fast discharging lithium-ion battery, *J. Energy Storage* 53 (2022) 105051.
- [8] K. Osmani, M. Alkhedher, M. Ramadan, D.S. Choi, L.K.B. Li, M.H. Doranehgard, et al., Recent progress in the thermal management of lithium-ion batteries, *J. Clean. Prod.* 389 (2023) 136024.
- [9] A. Habibi Khalaj, S.K. Halgamuge, A review on efficient thermal management of air- and liquid-cooled data centers: from chip to the cooling system, *Appl. Energy* 205 (2017) 1165–1188.
- [10] N. Putra, A.F. Sandi, B. Ariantara, N. Abdullah, T.M. Indra Mahlia, Performance of beeswax phase change material (PCM) and heat pipe as passive battery cooling system for electric vehicles, *Case Stud. Therm. Eng.* 21 (2020) 100655.
- [11] J. Bai, B. Zhang, B. Yang, J. Shang, Z. Wu, Preparation of three-dimensional interconnected graphene/ionic liquid composites to enhanced thermal conductivities for battery thermal management, *J. Clean. Prod.* 370 (2022) 133572.
- [12] M. Subramanian, A.T. Hoang, K. B. S. Nizetić, J.M. Solomon, D. Balasubramanian, et al., A technical review on composite phase change material based secondary assisted battery thermal management system for electric vehicles, *J. Clean. Prod.* 322 (2021) 129079.
- [13] Y. Ma, H. Yang, H. Zuo, Q. Zuo, X. He, W. Chen, et al., EG@Bi-MOF derived porous carbon/lauric acid composite phase change materials for thermal management of batteries, *Energy* 272 (2023) 127180.
- [14] W. Wu, W. Wu, S. Wang, Thermal optimization of composite PCM based large-format lithium-ion battery modules under extreme operating conditions, *Energy Conv. Manag.* 153 (2017) 22–33.
- [15] Z. Rao, S. Wang, A review of power battery thermal energy management, *Renew. Sust. Energ. Rev.* 15 (2011) 4554–4571.
- [16] M.N. Khan, H.A. Dhahad, S. Alamri, A.E. Anqi, K. Sharma, S. Mehrez, et al., Air cooled lithium-ion battery with cylindrical cell in phase change material filled cavity of different shapes, *J. Energy Storage* 50 (2022) 104573.
- [17] S. Ahmad, Y. Liu, S.A. Khan, M. Hao, X. Huang, Hybrid battery thermal management by coupling fin intensified phase change material with air cooling, *J. Energy Storage* 64 (2023) 107167.
- [18] Y. Yang, L. Chen, L. Yang, X. Du, Numerical study of combined air and phase change cooling for lithium-ion battery during dynamic cycles, *Int. J. Therm. Sci.* 165 (2021) 106968.
- [19] Z. Leng, Y. Yuan, X. Cao, W. Zhong, C. Zeng, Heat pipe/phase change material coupled thermal management in Li-ion battery packs: optimization and energy-saving assessment, *Appl. Therm. Eng.* 208 (2022) 118211.
- [20] R.D. Jilte, R. Kumar, M.H. Ahmadi, Cooling performance of nanofluid submerged vs. nanofluid circulated battery thermal management systems, *J. Clean. Prod.* 240 (2019) 118131.
- [21] Z. Rao, Q. Wang, C. Huang, Investigation of the thermal performance of phase change material/mini-channel coupled battery thermal management system, *Appl. Energy* 164 (2016) 659–669.
- [22] H. Liu, S. Ahmad, Y. Shi, J. Zhao, A parametric study of a hybrid battery thermal management system that couples PCM/copper foam composite with helical liquid channel cooling, *Energy* 231 (2021) 120869.
- [23] X. Liu, C.-F. Zhang, J.-G. Zhou, X. Xiong, C.-C. Zhang, Y.-P. Wang, Numerical simulation of hybrid battery thermal management system combining of thermoelectric cooler and phase change material, *Energy Rep.* 8 (2022) 1094–1102.
- [24] M.L. Hao, J. Li, S. Park, S. Moura, C. Dames, Efficient thermal management of Li-ion batteries with a passive interfacial thermal regulator based on a shape memory alloy, *Nat. Energy* 3 (2018) 899–906.
- [25] G. Liao, K. Jiang, F. Zhang, J. E. L. Liu, J. Chen, et al., Thermal performance of battery thermal management system coupled with phase change material and thermoelectric elements, *J. Energy Storage* 43 (2021) 103217.
- [26] X. Liu, C.-F. Zhang, J.-G. Zhou, X. Xiong, Y.-P. Wang, Thermal performance of battery thermal management system using fins to enhance the combination of thermoelectric cooler and phase change material, *Appl. Energy* 322 (2022) 119503.
- [27] D. Luo, Z. Wu, Y. Yan, J. Cao, X. Yang, Y. Zhao, et al., Performance investigation and design optimization of a battery thermal management system with thermoelectric coolers and phase change materials, *J. Clean. Prod.* 434 (2024) 139834.
- [28] L. Jiang, H. Zhang, J. Li, P. Xia, Thermal performance of a cylindrical battery module impregnated with PCM composite based on thermoelectric cooling, *Energy* 188 (2019) 116048.
- [29] W. Song, F. Bai, M. Chen, S. Lin, Z. Feng, Y. Li, Thermal management of standby battery for outdoor base station based on the semiconductor thermoelectric device and phase change materials, *Appl. Therm. Eng.* 137 (2018) 203–217.
- [30] F. Dong, Z. Cheng, J. Zhu, D. Song, J. Ni, Investigation and optimization on cooling performance of a novel double helix structure for cylindrical lithium-ion batteries, *Appl. Therm. Eng.* 189 (2021) 116758.
- [31] F. Zhang, L. Zhai, L. Zhang, M. Yi, B. Du, S. Li, A novel hybrid battery thermal management system with fins added on and between liquid cooling channels in composite phase change materials, *Appl. Therm. Eng.* 207 (2022) 118198.
- [32] R. Akula, C. Balaji, Thermal management of 18650 Li-ion battery using novel fins-PCM-EG composite heat sinks, *Appl. Energy* 316 (2022) 119048.
- [33] Y. Zhao, B. Zou, J. Ding, Y. Ding, Experimental and numerical investigation of a hybrid battery thermal management system based on copper foam-paraffin composite phase change material and liquid cooling, *Appl. Therm. Eng.* 218 (2023) 119312.
- [34] V. Mali, R. Saxena, K. Kumar, A. Kalam, B. Tripathi, Review on battery thermal management systems for energy-efficient electric vehicles, *Renew. Sust. Energ. Rev.* 151 (2021) 111611.

- [35] C. Pan, Z. Jia, J. Wang, L. Wang, J. Wu, Optimization of liquid cooling heat dissipation control strategy for electric vehicle power batteries based on linear time-varying model predictive control, *Energy* 283 (2023) 129099.
- [36] X. Cao, N. Zhang, Y. Yuan, X. Luo, Thermal performance of triplex-tube latent heat storage exchanger: simultaneous heat storage and hot water supply via condensation heat recovery, *Renew. Energy* 157 (2020) 616–625.
- [37] Y. Zhao, B. Zou, T. Zhang, Z. Jiang, J. Ding, Y. Ding, A comprehensive review of composite phase change material based thermal management system for lithium-ion batteries, *Renew. Sust. Energ. Rev.* 167 (2022) 112667.
- [38] D. Luo, Z. Sun, R. Wang, Performance investigation of a thermoelectric generator system applied in automobile exhaust waste heat recovery, *Energy* 238 (2022) 121816.
- [39] Z. Sun, D. Luo, R. Wang, Y. Li, Y. Yan, Z. Cheng, et al., Evaluation of energy recovery potential of solar thermoelectric generators using a three-dimensional transient numerical model, *Energy* 256 (2022) 124667.
- [40] Q.L. Yue, C.X. He, M.C. Wu, J.B. Xu, T.S. Zhao, Pack-level modeling of a liquid cooling system for power batteries in electric vehicles, *Int. J. Heat Mass Transf.* 192 (2022) 122946.
- [41] D. Luo, S. Yang, Y. Yan, J. Cao, B. Cao, Performance improvement of the automotive thermoelectric generator by extending the hot side area of the heat exchanger through heat pipes, *Energy Convers. Manag.* 310 (2024) 118472.
- [42] F. Yi, J. E. B. Zhang, H. Zuo, K. Wei, J. Chen, et al., Effects analysis on heat dissipation characteristics of lithium-ion battery thermal management system under the synergism of phase change material and liquid cooling method, *Renew. Energy* 181 (2022) 472–489.
- [43] Q. Xin, J. Xiao, T. Yang, H. Zhang, X. Long, Thermal management of lithium-ion batteries under high ambient temperature and rapid discharging using composite PCM and liquid cooling, *Appl. Therm. Eng.* 210 (2022) 118230.